crystals

MDPI

Article

Characterization of the Strain-Rate-Dependent Plasticity of Alloys Using Instrumented Indentation Tests

Ta-Te Chen [1,2], Ikumu Watanabe [1,2,*] and Tatsuya Funazuka [3]

[1] Graduate School of Science and Technology, University of Tsukuba, Tsukuba 305-8577, Japan; s1930121@u.tsukuba.ac.jp
[2] Research Center for Structural Materials, National Institute for Materials Science, 1-2-1 Sengen, Tsukuba 305-0047, Japan
[3] Faculty of Engineering, University of Toyama, 3190 Gofuku, Toyama 930-8555, Japan; funazuka@eng.u-toyama.ac.jp
* Correspondence: WATANABE.Ikumu@nims.go.jp

Abstract: Instrumented indentation tests are an efficient approach for the characterization of stress–strain curves instead of tensile or compression tests and have recently been applied for the evaluation of mechanical properties at elevated temperatures. In high-temperature tests, the rate dependence of the applied load appears to be dominant. In this study, the strain-rate-dependent plasticity in instrumented indentation tests at high temperatures was characterized through the assimilation of experiments with a simulation model. Accordingly, a simple constitutive model of strain-rate-dependent plasticity was defined, and the material constants were determined to minimize the difference between the experimental results and the corresponding simulations at a constant high temperature. Finite element simulations using a few estimated mechanical properties were compared with the corresponding experiments in compression tests at the same temperature for the validation of the estimated material responses. The constitutive model and determined material constants can reproduce the strain-rate-dependent material behavior under various loading speeds in instrumented indentation tests; however, the load level of computational simulations is lower than those of the experiments in the compression tests. These results indicate that the local mechanical responses evaluated in the instrumented indentation tests were not consistent with the bulk responses in the compression tests at high temperature. Consequently, the bulk properties were not able to be characterized using instrumented indentation tests at high temperature because of the scale effect.

Keywords: strain-rate-dependent plasticity; instrumented indentation test; finite elements; mechanical testing

Citation: Chen, T.-T.; Watanabe, I.; Funazuka, T. Characterization of the Strain-Rate-Dependent Plasticity of Alloys Using Instrumented Indentation Tests. *Crystals* **2021**, *11*, 1316. https://doi.org/10.3390/cryst11111316

Academic Editor: Umberto Prisco

Received: 30 July 2021
Accepted: 26 October 2021
Published: 28 October 2021

1. Introduction

A database of fundamental material properties is essential for effective utilization of existing materials and exploration of new materials. For structural materials, tensile and compression tests among various mechanical tests are the standard testing methods for the characterization of mechanical properties based on the stress–strain curve because of the simple stress state. However, material tests require considerable effort and time for specimen preparation and for conducting tests under various conditions.

Accordingly, instrumented indentation tests are an efficient approach for the evaluation of mechanical properties, such as effective elastic stiffness and hardness. These tests require less effort for specimen preparation and provide multiple results from a single specimen. In addition, the test method is applicable for the characterization of nano- and microscopic mechanical behaviors through the control of the magnitude of the applied load. Therefore, instrumented indentation tests have been widely employed in material science and engineering, e.g., the studies of scale-dependent plasticity [1–3], microscopic heterogeneity [4–6], and complex deformation mechanisms [7–9].

Recently, instrumented indentation tests at elevated temperatures have attracted considerable attention for the characterization of the temperature dependency of mechanical properties, which has the potential for efficiently obtaining material databases for the research and development of heat-resistant materials. In this context, Chen et al. [10] applied nanoscopic instrumented indentation tests at elevated temperatures to the high-throughput screening of alloy compositions in AlFeCrNiMn high-entropy alloy systems. In particular, high-temperature nanoindentation equipment has been developed in recent years. Suzuki and Ohmura [11] first reported high-temperature nanoindentation measurements up to 600 °C on silicon samples. Ruzic et al. [12,13] extended the maximum temperature to 800 °C under an inert atmosphere. Minnert et al. [14] developed an improved nanoindentation system and characterized the creep behavior of a nickel single crystal at temperatures up to 1100 °C.

In instrumented indentation tests at high temperatures (high-temperature indentation tests), strain-rate-dependent plasticity becomes dominant in comparison with those at room temperatures. Therefore, various studies have been conducted to characterize the creep properties based on the results of high-temperature indentation tests. Chu et al. [15] first reported the determination of the creep properties of β-Sn single crystals using an instrumented indentation test. Dean et al. [16] proposed an approach for characterizing the primary and secondary creep behaviors using a spherical indenter. Takagi et al. [17,18], Takagi and Fujiwara [19], and Fujiwara et al. [20] determined the creep characteristics of various alloys under several loading conditions of instrumented indentation tests using a conical indenter. In the above studies, the creep behavior under an applied load in an instrumented indentation test was examined to correlate the results with creep properties, requiring long tests with duration over 1 min. The duration of high-temperature indentation tests should be minimized to prevent the degradation of the specimen surface and the indenter tip [12]. In creep measurements, the loading and unloading processes are generally ignored. However, they must be considered in an instrumented indentation test with a short duration. The material response in these processes depends not only on strain-rate-dependent properties but also on other mechanical properties, including elastic stiffness, strength, and work hardening. Therefore, it is difficult to simultaneously characterize the mechanical properties.

In instrumented indentation tests at room temperature, various approaches have been proposed to estimate the stress–strain relationship corresponding to a tensile test from load–depth ($P-h$) curves. Because a unique stress–strain relationship cannot be estimated from the $P-h$ curve of a single indentation test using a standard sharp indenter [21–23], dual-indenter and sphere indenter methods were proposed to determine a unique set of material constants in a simple constitutive model. For instance, in dual-indenter methods [24–26], two sharp indenters with different apex angles were employed. By contrast, sphere indenter methods [27–29] are based on the nonlinear relationship between the indentation depth and cross-sectional area of the indentation. These approaches focus on the $P-h$ curves. Goto et al. [30,31] used topography around the indentation marks with $P-h$ curves in a single indentation test using a standard sharp indenter to determine the plastic properties. In the above-mentioned estimation approaches, the computational simulations of the instrumented indentation tests play an important role in reproducing the material behavior and determining the material constants of a constitutive model. The framework developed in instrumented indentation tests at room temperature is based on the strain-rate-independent plasticity. Therefore, it can be extended to high-temperature indentation tests by employing a strain-rate-dependent plasticity.

In this study, we developed an approach for estimation of strain-rate-dependent plasticity based on the results of the high-temperature indentation tests. Initially, the simple constitutive model used in existing approaches [25,26,30,31] was extended to a strain-rate-dependent format. Next, high-temperature indentation tests were performed under different loading rates for an aluminum alloy specimen. Subsequently, the material constants of the proposed constitutive model were determined to minimize the difference

between the experimental $P-h$ curves and the curves obtained from their corresponding finite element simulations, as shown in Section 4. Lastly, the estimated mechanical properties were validated using a compression test at the same temperature.

2. Finite Element Modeling

A constitutive model in a strain-rate-dependent format and a finite element model were defined for the following computational simulations of high-temperature indentation tests.

2.1. Strain-Rate-Dependent Constitutive Model

An isotropic elastoplastic constitutive model for alloys was employed, which was characterized by the Saint-Venant's elasticity and metal plasticity based on the von Mises yield criterion. The elasticity was set as strain-independent, whereas the plastic constitutive equation was defined in a strain-rate-dependent format. In this study, the equivalent stress–strain relationship is expressed as follows:

$$\begin{cases} \sigma^* = E^*\varepsilon^* & \text{if } \sigma^* < \sigma_Y \text{(elasticity)} \\ \sigma^* = K(\varepsilon^*)^n\Gamma(\dot{\xi}) & \text{if } \sigma^* = \sigma_Y \text{(elasto–visco–plasticity)}, \end{cases} \tag{1}$$

where σ^*, ε^*, E^*, σ_Y, K, n, Γ, and ξ are the von Mises stress norm, equivalent strain, equivalent elastic modulus, yield stress, plastic coefficient, work-hardening exponent, strain-rate function, and equivalent plastic strain, respectively. The equivalent strain and elastic modulus are defined as follows:

$$\varepsilon^* = \sqrt{\frac{2}{3}\text{dev}[\boldsymbol{\varepsilon}] : \text{dev}[\boldsymbol{\varepsilon}]} = \frac{\sigma^*}{E^*} + \xi \quad \text{and} \quad E^* = \frac{3E}{2(1+\nu)}, \tag{2}$$

where $\boldsymbol{\varepsilon}$, E, and ν are the strain tensor, Young's modulus, and Poisson's ratio, respectively. In this study, the strain-rate function was defined as

$$\Gamma(\dot{\xi}) = (1-\alpha) + \alpha\left(\frac{\dot{\xi}}{\dot{\xi}_0}\right)^m \qquad \alpha \in [0,\ 1], \tag{3}$$

where α, $\dot{\xi}_0$, and m are the viscoplastic ratio, reference strain rate, and strain-rate exponent, respectively. Then, Equation (1) can be written as

$$\sigma^* = \left(\frac{\sigma^*}{E^*} + \xi\right)^n \left\{(1-\alpha)K + \alpha K\left(\frac{\dot{\xi}}{\dot{\xi}_0}\right)^m\right\} = \left(\frac{\sigma^*}{E^*} + \xi\right)^n \left\{K_p + K_{vp}\dot{\xi}^m\right\}, \tag{4}$$

where $K_p = (1-\alpha)K$ and $K_{vp} = \alpha K\dot{\xi}_0^{-m}$. Thus, this constitutive model contains four strain-rate-independent and two strain-rate-dependent material constants at a high temperature: E, ν, K_p, n, K_{vp}, and m. The strain-rate-independent initial yield strength is formulated as $\sigma_Y = \left\{(E^*)^{-n}K_p\right\}^{\frac{1}{1-n}}$. At a high temperature, α can be assumed to be equal to one, i.e., $K_p \equiv 0$. In the special case, a pure-elastic state does not exist.

2.2. Finite Element Model of the Instrumented Indentation Test

A three-dimensional finite element model of a specimen and Berkovich indenter was constructed for the computational simulations of the instrumented indentation tests described in Section 3.2, as shown in Figure 1. A mirror symmetrical boundary condition was applied to the $X-Y$ plane along the center of the object, and the vertical displacement along the bottom of the finite element model was constrained. The finite element model contains 15,358 nodes and 14,138 eight-node hexahedral elements with reduced integration, in which the contact area between the specimen and indenter was discretized more finely than the other areas. The indenter was assumed to be a rigid body. The friction between

the indenter and the sample was not considered in this study because the effect of friction on the indentation results is insignificant in the case of Berkovich indenter [25]. The friction effect was confirmed to be minor in simulations of the instrumented indentation tests using the strain-rate-dependent plasticity. A load was applied to the top of the indenter. Quasi-static boundary value problems were solved using the applied load control with an implicit scheme.

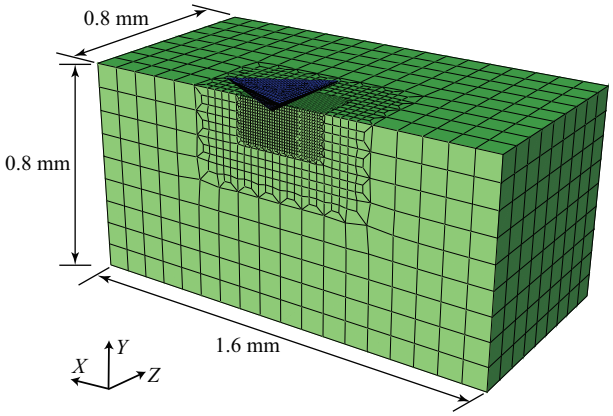

Figure 1. Finite element model of the instrumented indentation test.

2.3. Finite Element Model of the Compression Test

An axisymmetric finite element model was constructed for the computational simulations of the compression tests described in Section 3.2.1, as shown in Figure 2. The finite element model contained 990 nodes and 940 four-node quadrilateral and 4 three-node triangular axisymmetric elements, where triangular elements were employed for the corners of the specimen to avoid excessive distortion of the elements. The vertical displacement along the bottom of the finite element model was constrained. Coulomb friction model was employed, and its coefficient was calibrated as 0.16 to reproduce the experimental barreling deformation in the simulations.

Simulations were performed using displacement control at the top of the model and solved as quasi-static boundary value problems with an implicit scheme.

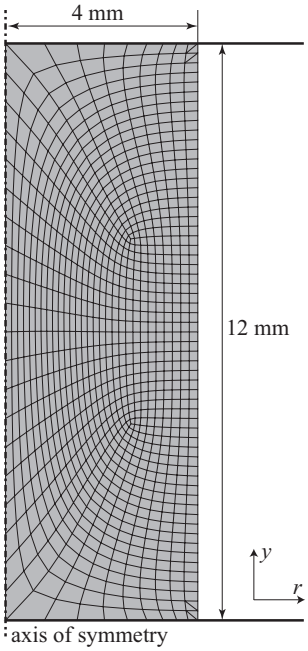

Figure 2. Finite element model of the compression tests.

3. Experiments

Experimental data were acquired to characterize and validate the strain-rate dependency of the plastic properties, where the instrumented indentation and compression tests at high temperature were performed at different test speeds.

3.1. Specimen

A wrought aluminum alloy with a grain size of approximately 200 μm was used in this study. The alloy composition is shown in Table 1. A melting temperature of a similar alloy (A7204) is 635 °C [32]. For instrumented indentation tests, mechanical polishing was conducted on the sample surface, followed by electrical polishing to remove the residual plastic strains.

Table 1. Alloy composition of the aluminum alloy [wt%].

Zn	Mg	Zr	Cu	Fe	Si	Ti
5.60	1.34	0.16	0.15	0.03	0.02	0.02

A tensile test at room temperature (approximately 20 °C) was performed, and the material constants of the constitutive model were determined under the assumption of an independent strain-rate ($\alpha \approx 0,\ m \approx 0$).

$$(E,\ \nu,\ K_{\mathrm{p}},\ n,) = (70\ \mathrm{GPa}, 0.3,\ 353.4\ \mathrm{MPa}, 0.08), \tag{5}$$

that also can be determined from the instrumented indentation tests [33]. The work-hardening exponent was approximately zero.

3.2. Instrumented Indentation Tests at High Temperatures

Instrumented indentation tests were performed at 300 °C using a diamond Berkovich indenter with the TI 950 TriboIndenter and xSol High-Temperature Stage (Bruker, Billerica, MA, USA), preventing the degradation of the specimen surface and indenter tip in the measurements in an inert argon atmosphere. The following experimental procedure for high-temperature indentation tests was established in our previous study [12].

After passively preheating the indenter tip at 300 °C, the instrumented indentation tests were performed for a maximum applied load of 1.5 N. The applied load was applied with three different load rates, i.e., 0.1, 1.0, and 10 N/s, with the unloading rate set to 0.1 N/s for each case after 10 s holding time at the maximum load. The indentation tests were performed five times for each condition to ensure reproducibility. The impressions of high-temperature indentation tests in loading rates of 0.1 and 10 N/s are shown in Figure 3, which were observed with a scanning electron microscopy (JSM-7001F, JEOL Ltd., Tokyo, Japan). According to these figures, the indentation tests were performed without crack, and no significant difference between them was found in the impressions.

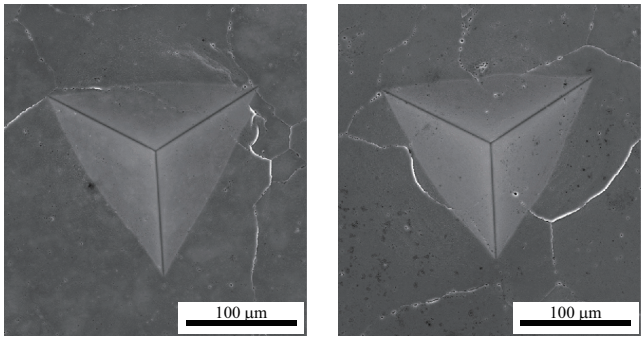

(**a**) 0.1 N/s (**b**) 10 N/s

Figure 3. Impressions of high-temperature indentation tests in loading rates of 0.1 and 10 N/s.

3.2.1. Compression Tests at High Temperatures

For the validation of the estimated material response, compression tests of the aluminum alloy were performed at three different test speeds (1.20, 0.12, and 0.06 mm/s; 0.10, 0.01, and 0.005/s in strain rate) in a chamber heated at 300 °C. Cylindrical samples (12 mm height, 8 mm diameter) corresponding to Figure 2 were compressed in the axial direction under displacement control using a precision Autograph AG-X Series universal tester (Shimadzu, Kyoto, Japan). The sample surface was lubricated to minimize bulging deformation in these tests.

4. Characterization of Strain Rate Dependency

In this section, material constants of the strain-rate-dependent plasticity were determined to minimize the difference between experiments and its computational simulations in high-temperature indentation tests. Moreover, the material response based on the constitutive model and the determined material constants was validated in compression tests at the same temperature.

4.1. Determination of Material Constants

The material constants were determined to minimize the difference in the $P-h$ curves between the experiments and the corresponding simulations for three loading speeds. In this study, the elastic constants E and ν at 300 °C were obtained from the literature [34] as 59 GPa and 0.35, respectively. The work-hardening exponent n was assumed to be 0.08, which is considered identical to that of the tensile test at room temperature for simplicity. Thus, the optimization problem is defined as follows:

$$\begin{aligned} &\text{minimize}\left[\Delta(K_{\mathrm{p}},\ K_{\mathrm{vp}},\ m)\right], \\ &\Delta := \sum_{i=1}^{N_{\mathrm{case}}} \left\{ \frac{1}{h_i^{\mathrm{exp,eh}}} \left(\left| h_i^{\mathrm{exp,bh}} - h_i^{\mathrm{sim,bh}} \right| + \left| h_i^{\mathrm{exp,eh}} - h_i^{\mathrm{sim,eh}} \right| \right) \right\}, \end{aligned} \tag{6}$$

where $h_i^{\mathrm{exp,bh}}$, $h_i^{\mathrm{exp,eh}}$, $h_i^{\mathrm{sim,bh}}$, and $h_i^{\mathrm{sim,eh}}$ are the indentation depths at the beginning and end of the holding process in the experimental and simulation results of the i-th case, respectively. N_{case} is the number of the loading rate cases. In this study, $N_{\mathrm{case}} = 3$, as specified in Section 3.2. Δ is the difference between the experimental and simulated $P-h$ curves.

In the both cases of $\alpha \in (0,1)$ and $\alpha = 1$, the sets of material constants were determined to solve the optimization problem (Equation (6)) using the Levenberg–Marquardt method [35] as follows:

$$\begin{aligned} &\alpha \in (0,1): \quad (K_{\mathrm{p}},\ K_{\mathrm{vp}},\ m) = (17.4\ \mathrm{MPa},\ 115.5\ \mathrm{MPa},\ 0.2367), \\ &\alpha = 1: \qquad\qquad\quad (K_{\mathrm{vp}},\ m) = (120.0\ \mathrm{MPa},\ 0.160), \end{aligned} \tag{7}$$

where Δ was 0.0731 for $\alpha \in (0,1)$ and 0.0784 for $\alpha = 1$. For $\alpha \in (0,1)$, the strain-rate-independent initial yield strength is calculated as $\sigma_{\mathrm{Y}} = 8.48$ MPa. Although the strength is non-negligible, the appropriate material constants can be found even in the case of $\alpha = 1$ (under the constraint of $K_{\mathrm{p}} \equiv 0$).

The $P-h$ curves obtained in the experiments and simulations using the determined material constants are shown in Figure 4. Additionally, the relationship between the depth and time during the holding process at the maximum applied load is shown in Figure 5. The strain-rate-dependent deformation behavior in the instrumented indentation tests was reproduced in computational simulations using the constitutive model in both cases.

From the results of the finite element analyses in the case of $\alpha \in (0,1)$, the distributions of Mises stress and equivalent plastic strain at the beginning and end of the holding processes for the loading rates of 0.1 and 10 N/s are shown in Figures 6 and 7, respectively. In the beginning of the holding process at the maximum applied load, the stress concentration around the indenter tip was observed in the case of a high loading rate, whereas the stress

distribution was uniform in the case of a slow loading rate due to the relaxation provided by the strain-rate-dependent deformation during the loading process. In addition, the distributions of an equivalent plastic strain before and after the holding process exhibit the evolution of the equivalent plastic strain during the holding process, which is more prominent in the case of a high loading rate.

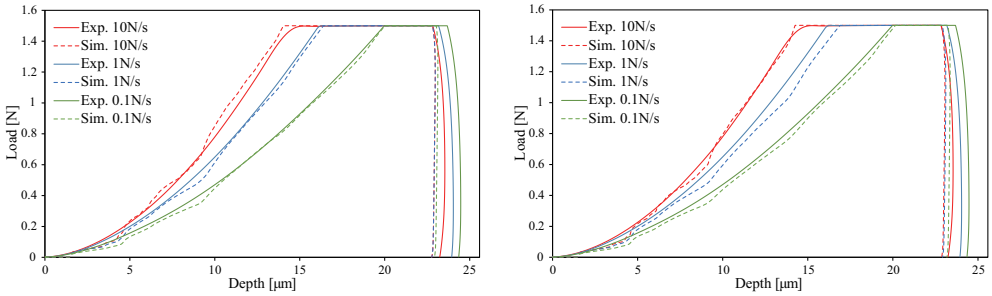

(**a**) $\alpha \in (0, 1)$ (**b**) $\alpha = 1$

Figure 4. Load–depth curves obtained in the experiments and simulations using the determined material constants. The dashed lines indicate the simulation results.

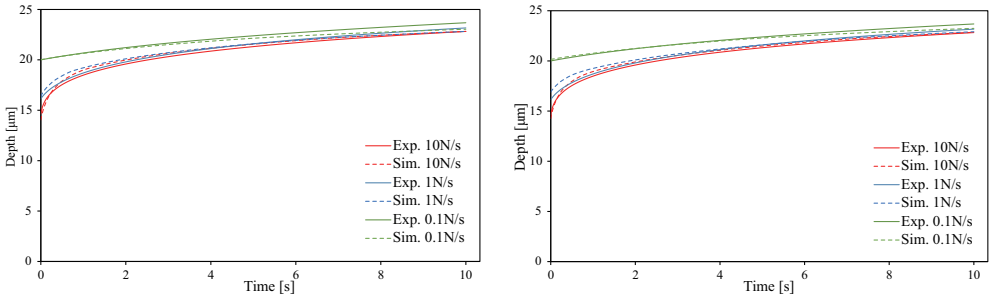

(**a**) $\alpha \in (0, 1)$ (**b**) $\alpha = 1$

Figure 5. Depth–time curves obtained in the experiments and simulations using the determined material constants. The dashed lines indicate the simulation results.

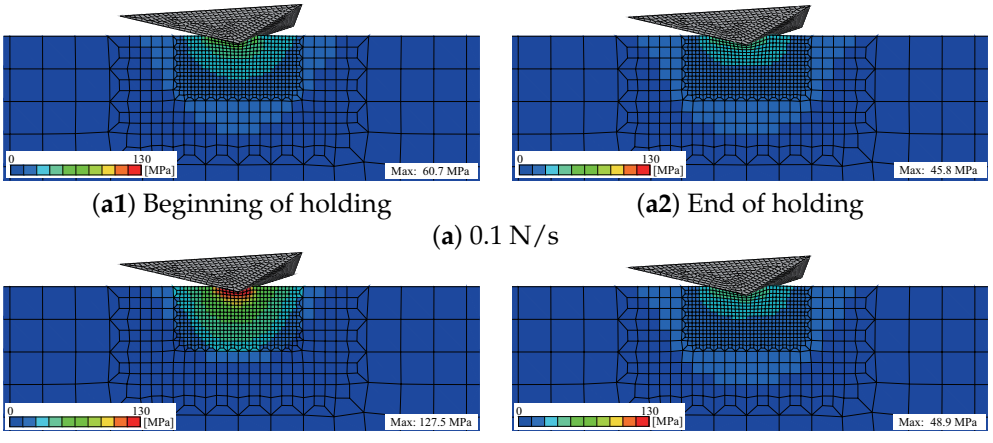

(**a1**) Beginning of holding (**a2**) End of holding

(**a**) 0.1 N/s

(**b1**) Beginning of holding (**b2**) End of holding

(**b**) 10 N/s

Figure 6. von Mises stress distribution at the beginning and end of the holding processes in the computational simulations using the determined material constants for $\alpha \in (0, 1)$.

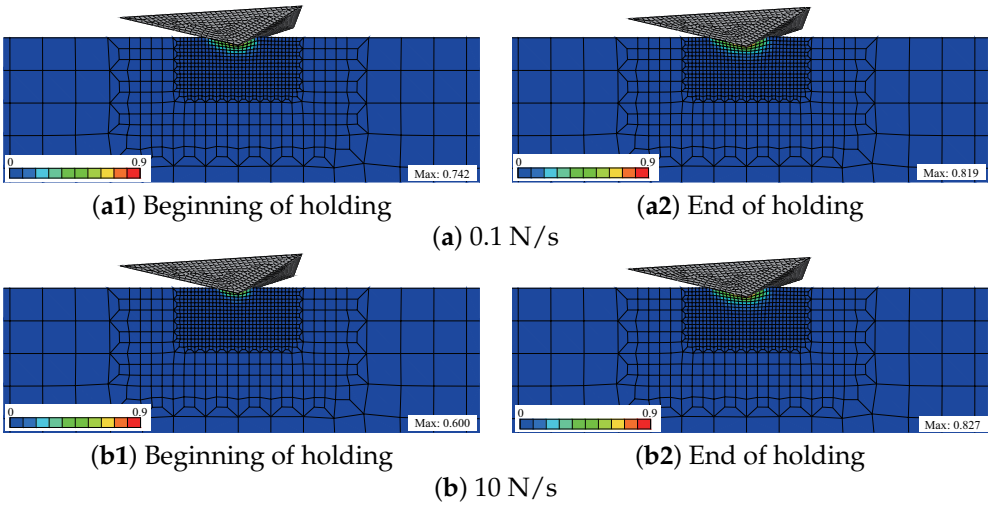

(**a1**) Beginning of holding (**a2**) End of holding

(**a**) 0.1 N/s

(**b1**) Beginning of holding (**b2**) End of holding

(**b**) 10 N/s

Figure 7. Equivalent plastic strain distribution at the beginning and end of the holding processes in the computational simulations using the determined material constants for $\alpha \in (0, 1)$.

4.2. Validation in Compression Tests

Using the constitutive model (Equation (4)) and determined material constants (Equation (7)), computational simulations of the compression tests at three test speeds (1.20, 0.12, and 0.06 mm/s) were performed. The load–stroke curves obtained from the experiments and simulations at 300 °C are shown in Figure 8. The results indicate that the load levels of the simulations are less consistent than those of the experiments, although the strain-rate-dependent material responses were characterized in the computational simulations. In other words, the constitutive model is applicable for reproducing the material behavior at high temperature; however, the material responses evaluated in the instrumented indentation tests did not agree with those obtained in the compression tests.

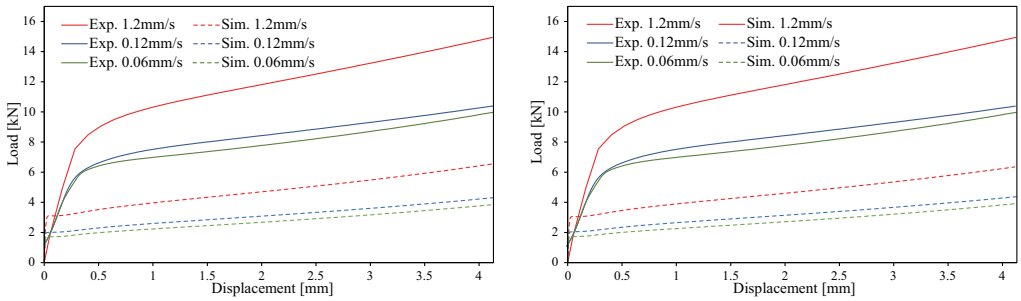

(**a**) $\alpha \in (0, 1)$ (**b**) $\alpha = 1$

Figure 8. Load–stroke curves in the experiments and simulations using the determined material constants. The dashed lines indicate the simulation results.

The critical difference between the instrumented indentation test and bulk test is the scale of the deformation domain. In the instrumented indentation tests, the influence region of the residual stress and plastic deformation is estimated as smaller than a hemisphere with a radius of 500 μm as shown in Figures 6 and 7; i.e., the evaluation domain contained a few crystal grains. Therefore, the instrumented indentation tests were not carried out for a polycrystal. This can be considered as an origin of the discrepancy. In fact, distinctive material behaviors at high temperature such as grain boundary sliding were reported in aluminum alloys [36,37]. The microscopic heterogeneity does not have a significant effect at room temperature [30,31,33]; however, the discrepancy arises particularly at high temperature. The scale and temperature effects require further investigations.

5. Conclusions

A new estimation approach for strain-rate-dependent plasticity was developed based on the instrumented indentation tests, where the material constants of the strain-rate-dependent constitutive model were determined from the results of experiments and the corresponding computational simulations at different test speeds. This approach can estimate the strain-rate-dependency of the material response in high-temperature indentation tests; however, the estimated mechanical properties were not consistent with the results of the compression tests. The estimation of bulk properties using high-temperature indentation tests remains an unsolved problem.

In this study, we focused on the material behavior of one alloy sample under the isothermal single condition. Through a systematic examination of various samples and thermal conditions, the microstructure and temperature dependencies can also be characterized using the proposed approach.

Author Contributions: Conceptualization, data curation, formal analysis, methodology, software, investigation, writing—original draft preparation, and visualization, T.-T.C. and I.W.; resources and validation, T.-T.C., I.W. and T.F.; writing—review and editing, supervision, project administration, and funding acquisition, I.W. All authors have read and agreed to the published version of the manuscript.

Funding: This research was funded by JSPS KAKENHI [grant number 21H01220] and Amada Foundation for Metal Work Technology [grant number AF-2018035-C2].

Institutional Review Board Statement: Not applicable.

Informed Consent Statement: Not applicable.

Data Availability Statement: Not applicable.

Acknowledgments: The authors wish to acknowledge Y. Yamamoto, E. Nakagawa, D. Araki, and H. Murakami of the National Institute for Materials Science for their technical support.

Conflicts of Interest: The authors declare no conflict of interest.

References

1. Spary, I.; Bushby, A.; Jennett, N.M. On the indentation size effect in spherical indentation. *Philos. Mag.* **2006**, *86*, 5581–5593. [CrossRef]
2. Rester, M.; Motz, C.; Pippan, R. Indentation across size scales–A survey of indentation-induced plastic zones in copper {1 1 1} single crystals. *Scr. Mater.* **2008**, *59*, 742–745. [CrossRef]
3. Fincher, C.D.; Ojeda, D.; Zhang, Y.; Pharr, G.M.; Pharr, M. Mechanical properties of metallic lithium: from nano to bulk scales. *Acta Mater.* **2020**, *186*, 215–222. [CrossRef]
4. Ruzic, J.; Emura, S.; Ji, X.; Watanabe, I. Mo segregation and distribution in Ti–Mo alloy investigated using nanoindentation. *Mater. Sci. Eng. A* **2018**, *718*, 48–55. [CrossRef]
5. Hintsala, E.D.; Hangen, U.; Stauffer, D.D. High-throughput nanoindentation for statistical and spatial property determination. *JOM* **2018**, *70*, 494–503. [CrossRef]
6. Matsuno, T.; Ando, R.; Yamashita, N.; Yokota, H.; Goto, K.; Watanabe, I. Analysis of preliminary local hardening close to the ferrite–martensite interface in dual-phase steel by a combination of finite element simulation and nanoindentation test. *Int. J. Mech. Sci.* **2020**, *180*, 105663. [CrossRef]
7. Li, K.; Injeti, V.; Misra, R.; Cai, Z.; Ding, H. On the strain rate sensitivity of aluminum-containing transformation-induced plasticity steels: Interplay between TRIP and TWIP effects. *Mater. Sci. Eng. A* **2018**, *711*, 515–523. [CrossRef]
8. Man, T.; Ohmura, T.; Tomota, Y. Mechanical behavior of individual retained austenite grains in high carbon quenched-tempered steel. *ISIJ Int.* **2019**, *59*, 559–566. [CrossRef]
9. Man, T.; Ohmura, T.; Tomota, Y. The effect of boundary or interface on stress-induced martensitic transformation in a Fe-Ni alloy. *Mater. Today Commun.* **2020**, *23*, 100896. [CrossRef]
10. Chen, Y.; Hintsala, E.; Li, N.; Becker, B.R.; Cheng, J.Y.; Nowakowski, B.; Weaver, J.; Stauffer, D.; Mara, N.A. High-throughput nanomechanical screening of phase-specific and temperature-dependent hardness in AlxFeCrNiMn high-entropy alloys. *JOM* **2019**, *71*, 3368–3377. [CrossRef]
11. Suzuki, T.; Ohmura, T. Ultra-microindentation of silicon at elevated temperatures. *Philos. Mag. A* **1996**, *74*, 1073–1084. [CrossRef]
12. Ruzic, J.; Watanabe, I.; Goto, K.; Ohmura, T. Nano-indentation measurement for heat resistant alloys at elevated temperatures in inert atmosphere. *Mater. Trans.* **2019**, *60*, 1411–1415. [CrossRef]

13. Ruzic, J.; Goto, K.; Watanabe, I.; Osada, T.; Wu, L.; Ohmura, T. Temperature-dependent deformation behavior of γ and *gamma'* single-phase nickel-based superalloys. *Mater. Sci. Eng. A* **2021**, *818*, 141439. [CrossRef]
14. Minnert, C.; Oliver, W.C.; Durst, K. New ultra-high temperature nanoindentation system for operating at up to 1100 °C. *Mater. Des.* **2020**, *192*, 108727. [CrossRef]
15. Chu, S.; Li, J. Impression creep of β-tin single crystals. *Mater. Sci. Eng.* **1979**, *39*, 1–10. [CrossRef]
16. Dean, J.; Bradbury, A.; Aldrich-Smith, G.; Clyne, T. A procedure for extracting primary and secondary creep parameters from nanoindentation data. *Mech. Mater.* **2013**, *65*, 124–134. [CrossRef]
17. Takagi, H.; Dao, M.; Fujiwara, M.; Otsuka, M. Experimental and computational creep characterization of Al–Mg solid-solution alloy through instrumented indentation. *Philos. Mag.* **2003**, *83*, 3959–3976. [CrossRef]
18. Takagi, H.; Dao, M.; Fujiwara, M. Analysis on pseudo-steady indentation creep. *Acta Mech. Solida Sin.* **2008**, *21*, 283–288. [CrossRef]
19. Takagi, H.; Fujiwara, M. Set of conversion coefficients for extracting uniaxial creep data from pseudo-steady indentation creep test results. *Mater. Sci. Eng. A* **2014**, *602*, 98–104. [CrossRef]
20. Fujiwara, M.; Takagi, H.; Higashida, K. High-temperature creep mechanism of dual-ductile-phase magnesium alloy with long-period stacking ordered phase. *Mater. Trans.* **2019**, *60*, 503–512. [CrossRef]
21. Cheng, Y.T.; Cheng, C.M. Can stress–strain relationships be obtained from indentation curves using conical and pyramidal indenters? *J. Mater. Res.* **1999**, *14*, 3493–3496. [CrossRef]
22. Tho, K.K.; Swaddiwudhipong, S.; Liu, Z.S.; Zeng, K.; Hua, J. Uniqueness of reverse analysis from conical indentation tests. *J. Mater. Res.* **2004**, *19*, 2498–2502. [CrossRef]
23. Alkorta, J.; Martinez-Esnaola, J.M.; Sevillano, J.G. Absence of one-to-one correspondence between elastoplastic properties and sharp-indentation load–penetration data. *J. Mater. Res.* **2005**, *20*, 432–437. [CrossRef]
24. Futakawa, M.; Wakui, T.; Tanabe, Y.; Ioka, I. Identification of the constitutive equation by the indentation technique using plural indenters with different apex angles. *J. Mater. Res.* **2001**, *16*, 2283–2292. [CrossRef]
25. Bucaille, J.L.; Stauss, S.; Felder, E.; Michler, J. Determination of plastic properties of metals by instrumented indentation using different sharp indenters. *Acta Mater.* **2003**, *51*, 1663–1678. [CrossRef]
26. Chollacoop, N.; Dao, M.; Suresh, S. Depth-sensing instrumented indentation with dual sharp indenters. *Acta Mater.* **2003**, *51*, 3713–3729. [CrossRef]
27. Taljat, B.; Zacharia, T.; Kosel, F. New analytical procedure to determine stress–strain curve from spherical indentation data. *Int. J. Solids Struct.* **1998**, *35*, 4411–4426. [CrossRef]
28. Ahn, J.H.; Kwon, D. Derivation of plastic stress–strain relationship from ball indentations: Examination of strain definition and pileup effect. *J. Mater. Res.* **2001**, *16*, 3170–3178. [CrossRef]
29. Swadener, J.; Taljat, B.; Pharr, G. Measurement of residual stress by load and depth sensing indentation with spherical indenters. *J. Mater. Res.* **2001**, *16*, 2091–2102. [CrossRef]
30. Goto, K.; Watanabe, I.; Ohmura, T. Determining suitable parameters for inverse estimation of plastic properties based on indentation marks. *Int. J. Plast.* **2019**, *116*, 81–90. [CrossRef]
31. Goto, K.; Watanabe, I.; Ohmura, T. Inverse estimation approach for elastoplastic properties using the load-displacement curve and pile-up topography of a single Berkovich indentation. *Mater. Des.* **2020**, *194*, 108925. [CrossRef]
32. Duan, Y.; Xu, J.; Chen, J.; Yu, C.; Chen, J.; Lu, H. The effects of heat treatment on the microstructure and cyclic behavior of A7N01-T4 aluminum alloy. *Mater. Charact.* **2017**, *131*, 201–209. [CrossRef]
33. Chen, T.; Watanabe, I.; Liu, D.; Goto, K. Data-driven estimation of plastic properties of alloys using neighboring indentation test. *Sci. Technol. Adv. Mater. Methods* **2021**, *1*, 143–151.
34. Simmons, G.; Wang, H. *Single Crystal Elastic Constants and Calculated Aggregate Properties*; MIT Press: Cambridge, MA, USA, 1971.
35. Marquardt, D.W. An algorithm for least-squares estimation of nonlinear parameters. *J. Soc. Ind. Appl. Math.* **1963**, *11*, 431–441. [CrossRef]
36. Lüthy, H.; White, R.A.; Sherby, O.D. Grain boundary sliding and deformation mechanism maps. *Mater. Sci. Eng.* **1979**, *39*, 211–216. [CrossRef]
37. Cipoletti, D.E.; Bower, A.F.; Qi, Y.; Krajewski, P.E. The influence of heterogeneity in grain boundary sliding resistance on the constitutive behavior of AA5083 during high-temperature deformation. *Mater. Sci. Eng. A* **2009**, *504*, 175–182. [CrossRef]